

Diagnosing and Predicting ENSO SSTA Development from Moored-Buoy and Scatterometer Winds

ANDREW M. CHIODI

Joint Institute for the Study of the Ocean and Atmosphere, University of Washington, and NOAA/Pacific Marine Environmental Laboratory, Seattle, Washington

(Manuscript received 5 March 2019, in final form 7 August 2019)

ABSTRACT


Accurate real-time knowledge of equatorial Pacific wind stress is critical for monitoring the state of the tropical Pacific Ocean and understanding sea surface temperature anomaly (SSTA) development associated with El Niño–Southern Oscillation (ENSO) events. The tropical Pacific moored-buoy array has been shown to adequately provide this knowledge when operating as designed. Ocean model simulation of equatorial Pacific SSTA by moored-buoy winds reveals that recent western Pacific buoy losses exceed the array's minimal redundancy. Additional wind measurements are needed to adequately simulate ENSO-related SSTA development when large portions of the moored-buoy array have been lost or decommissioned. Prospects for obtaining this supplemental wind information in real time are evaluated from simulations of central equatorial Pacific SSTA development during 2017 and end-of-year Niño-3.4 conditions during the previous 25 years. Results show that filling multiple-buoy-dropout gaps with winds from a pair of scatterometers (2000–17) achieves simulation accuracy improving upon that available from the moored-buoy array in the case in which large portions of the array are out. Forcing with the reanalysis-product winds most commonly used in recent ENSO studies or the scatterometer measurements (without the buoy winds) degrades simulation accuracy. The utility of having accurate basinwide wind stress information is demonstrated in an examination of the role that easterly weather-scale wind events played in driving the unexpected development of La Niña in 2017 and by showing that wintertime Niño-3.4 conditions can be statistically forecast, with skill comparable to state-of-the-art coupled models, on the basis of accurate knowledge of equatorial Pacific wind variability over spring or summer.


1. Introduction

Equatorial Pacific zonal wind stress variability is a dominant driver of the equatorial Pacific sea surface temperature anomaly (SSTA) development associated with El Niño–Southern Oscillation (ENSO) events. In both their warm-SSTA (El Niño) and cool-SSTA (La Niña) extremes, ENSO events can significantly influence seasonal weather conditions in affected regions around Earth. The strongest and most consistent ENSO

associations with extratropical seasonal weather anomalies generally occur in boreal winter (Trenberth et al. 1998; Wolter et al. 1999; Sarachik and Cane 2010; Chiodi and Harrison 2013, 2015b). The prevalence of one ENSO extreme over the other during a multiyear span (e.g., La Niña becoming more frequent than El Niño) has been found to be a precursor of multiyear drought in affected extratropical regions (Schubert et al. 2004; Seager et al. 2005; Herweijer et al. 2006). Accurate real-time knowledge of equatorial Pacific wind variability is critical for monitoring the coupled-anomaly state of the tropical Pacific. It also provides the basis for initialization and verification of coupled ocean–atmosphere forecast models.

Wind observations from the tropical Pacific moored-buoy array [also known as TAO/Triangle Trans-Ocean Buoy Network (TRITON)] provide high-quality real-time wind observations from ~70 mooring sites that span the equatorial basin from 8°S to 8° or 9°N and from 137°E to 95°W (McPhaden et al. 1998). The interbuoy spacing of TAO/TRITON was designed to resolve the

 Denotes content that is immediately available upon publication as open access.

 Supplemental information related to this paper is available at the Journals Online website: <https://doi.org/10.1175/JCLI-D-19-0183.s1>.

Corresponding author: Andrew M. Chiodi, andy.chiodi@noaa.gov

DOI: 10.1175/JCLI-D-19-0183.1

© 2019 American Meteorological Society. For information regarding reuse of this content and general copyright information, consult the [AMS Copyright Policy](#) (www.ametsoc.org/PUBSReuseLicenses).

meridional and zonal coherence length scales of equatorial Pacific wind variability on time scales greater than 2 days, as they were determined based on tropical Pacific island wind records by [Harrison and Luther \(1990\)](#).

TAO/TRITON has recently been confirmed to work as designed to provide basinwide wind observations for forcing ocean model simulations of observed central equatorial Pacific SSTA development and thereby providing a basis for understanding that development. In fact, the simulations of Niño-3.4 SSTA development forced by the moored-buoy winds on their own have been found to be substantially more accurate than those driven by the reanalysis wind stress products used most commonly in recent ENSO studies over the first 20 years of the array (1992–2011; [Chiodi and Harrison 2017a](#)).

The usefulness of the array is conditional, however, on there being few gaps caused by nonfunctioning buoys ([Chiodi and Harrison 2017b](#)). The aforementioned coherence length-based array design suggests that the gap caused by a nonfunctioning buoy surrounded by operational ones can be filled with reasonable confidence based on the adjacent mooring wind observations. But when adjacent buoys are also out, wind information is lost from the array.

Currently, only 2 of the traditional 12 TRITON buoys (sites along 137°, 147°, and 156°E) are reporting wind observations. This creates large gaps in buoy coverage over the far western tropical Pacific, which is a locus of westerly wind events known to play a key role in the onset and development of El Niño events ([Vecchi and Harrison 2000](#); [Lengaigne et al. 2004](#); [Lopez and Kirtman 2014](#)). Failure to find other means by which wind and wind stress variability can be accurately estimated over this region would result in a substantial decrease in our ability to monitor ENSO state and understand the reasons for observed ENSO-related SSTA developments.

Here we examine the prospects for filling the wind knowledge gaps caused by buoy dropouts with other sources of wind information that are available in real or near-real time. Sources of wind information considered herein include the direct observations provided by the Tropical Pacific moorings (with and without lost-buoy gap filling by cross-buoy interpolation), measurements from a pair of satellite-based scatterometers; namely, QuikSCAT from 2000 to 2009 and ASCAT-A from 2009 to 2017 (expansions of many of the acronyms used in this paper can be found at <https://PubsAcronymList>), and a popular numerical weather model run in data assimilation mode: the NCEP–NCAR reanalysis (NCEP-1; [Kalnay et al. 1996](#)). NCEP-1 is chosen in this case because it is distinct among other popular reanalysis wind products for offering real-time availability.

We evaluate different waveguide-wide wind stress compilations by their respective ability to force an ocean general circulation model to accurately simulate observed Niño-3.4 behavior. Accuracy is evaluated based on the root-mean-square error (RMSE) between observed end-of-year Niño-3.4 conditions and those simulated in a series of yearlong model runs. Annual simulations date back to 1992 for wind stress fields that do not include satellite information, and 2000 that do.

The simulation experiments performed for this examination are configured using the popular Geophysical Fluid Dynamics Laboratory (GFDL) Modular Ocean Model (specifically, MOM4p1; [Griffies et al. 2003](#)) and are free forced, as in [Chiodi and Harrison \(2017a,b\)](#), meaning that no form of model nudging toward observed ocean temperature is applied. If the applied wind stress is inaccurate, the ocean model is deficient, or something other than wind stress is responsible for the observed SSTA development, the model simulation will be inaccurate. If accurate SSTA development is simulated in this model configuration, this is an indication that wind forcing provided a dominant control on the observed SSTA development and that our observing system provided usefully accurate knowledge of that wind forcing.

After evaluating each wind stress compilation's ability to force accurate SSTA simulations in the ocean model, the utility of the top-performing wind stress field is explored in two contexts. One is a case study of the role of subseasonal wind events in driving the 2017 La Niña. The other is as a statistical predictor of wintertime Niño-3.4 conditions (the dynamical ocean model is not incorporated in the statistical forecasting context).

The ENSO development trajectory observed in 2017 exhibited some weak El Niño-like characteristics in summer (moderately warm central equatorial Pacific SSTAs) but then surprised forecasters by reaching La Niña SSTA status by the end of the year. Understanding the reasons for this unexpected midyear reversal in development is an important first step toward improving upon our ability to predict event developments like this one. The best-performing wind stress compilation is able to simulate the observed midyear reversal in development with timing and amplitude like that observed, achieving a signal-to-noise ratio of ~ 3 based on the RMSE of the simulated monthly 2017 Niño-3.4 values and the standard deviation of the observed 2017 Niño-3.4 trajectory. Based on this wind stress compilation, the distribution of subseasonal wind events in 2017 is identified using the detection algorithm of [Chiodi and Harrison \(2015a\)](#). Subsequent model experiments are performed to examine the role that the observed wind event distribution played in the mid-2017 reversal in ENSO SSTA development.

Skill in predicting Niño-3.4 SSTA conditions at leads of a few months to seasons has been (Kumar et al. 2007; Xue et al. 2013) and remains (Barnston et al. 2019) a much-scrutinized benchmark for our ability to forecast ENSO. The basis for predicting boreal wintertime Niño-3.4 anomaly from accurate knowledge of equatorial Pacific wind variability is revisited herein using a statistical forecasting approach based on the best-performing wind stress field over the period for which winds from both the moored-buoy array and scatterometers are available (2000–17). In this case, equatorial Pacific wind stress is arithmetically integrated over different (boreal) spring, summer and fall periods and then used as a predictor for the subsequent wintertime Niño-3.4 SSTA anomaly. The retrospective forecast skill of the wind stress–integral approach is compared with that offered by the NCEP Climate Forecast System, version 2 (CFSv2; Saha et al. 2010).

The presentation of results herein is organized as follows. The methods used to construct equatorial Pacific waveguide-wide wind stress fields based on mooring and scatterometer winds are described in section 2. Ocean modeling methods are also described in section 2. Model simulations of the 2017 Niño-3.4 development trajectory forced by the different candidate wind stress datasets are examined in section 3. The role of easterly wind surges (EWS) in driving the observed Niño-3.4 development in 2017 is further examined in section 4. End-of-year Niño-3.4 simulation accuracy over the period 1992–2017 is examined in section 5. The prospects for statistically predicting boreal wintertime Niño-3.4 conditions based on wind stress integrals over the preceding seasons are examined in section 6. Discussion and conclusions are offered in section 7.

2. Data and methods

Near-surface wind data were acquired from TAO/TRITON (TAO/TRITON 2000), which provides direct daily-averaged wind observations, in real time, from ~70 sites spanning the equatorial Pacific Ocean waveguide along the longitudes of 137°E, 147°E, 156°E, 165°E, 180°, 170°W, 155°W, 140°W, 125°W, 110°, and 95°W, and latitudes of 8°S, 5°S, 2°S, 0°, 2°N, 5°N, and 8°N (or 9°N at 140°W). Daily-averaged moored-buoy winds, themselves calculated from the 10-min averages collected and stored on the buoys, were obtained from the NOAA Pacific Marine Environmental Laboratory TAO project office. Data from individual equatorial sites date back to the early 1980s, but the study period herein starts in 1992, when annually-averaged data return over the core ocean waveguide (2°S–2°N) first reached 60% relative to perfect return from the array as it was designed. Chiodi and Harrison (2017a) found the 60% return level

to be the minimum necessary for adequate ocean-model simulation of observed Niño-3.4 SSTA development.

Wind data are converted to zonal pseudostress τ^x using the following formula:

$$\tau^x = \rho_a C_d |\mathbf{U}| u,$$

with air density ρ_a assigned the value of 1.25 kg m^{-3} , $C_d = 1.3 \times 10^{-3}$, \mathbf{U} being the 10-m wind vector, and u its zonal component. Buoy winds observed at 4 m above sea level were adjusted to 10-m height using a logarithmic height adjustment and assuming neutral atmospheric stability (also done in Mears et al. 2001) with $1.52 \times 10^{-4} \text{ m}$ as the oceanic surface roughness length (Peixoto and Oort 1992). In the case of 4-m mooring wind measurements, this equates to multiplying the mooring wind speeds by 1.09 to adjust them to the nominal height (10 m) of the satellite- and reanalysis-based wind data described below.

Wind stress anomalies are calculated by subtracting the monthly-mean seasonal cycle (also known as climatology) for the 1992–2017 period, with daily climatological values determined based on linear interpolation of the monthly climatological means. This anomaly definition is used for all variables considered herein, including SST, with the limitation in the scatterometer wind case that the record begins in late 1999 (discussed below).

For subseasonal near-surface equatorial Pacific wind event identification, we use the detection algorithm of Chiodi and Harrison (2015a). By this method, wind events are identified when daily- and waveguide-averaged (5°S–5°N) zonal wind stress anomalies exceed 0.045 Pa in magnitude (easterly or westerly) over at least 25° of longitude and three, or more, consecutive days. The region over which the anomaly exceeds the threshold may differ by day but must overlap the previous such region. This feature of the detection algorithm allows events to grow in zonal length or propagate eastward/westward.

By design, TAO/TRITON moorings are spaced to match the coherence length scales of the wind variability on time scales greater than a few days (Harrison and Luther 1990). To synthesize a waveguide-wide wind stress field based on the TAO/TRITON wind observations, we take advantage of this design feature and subdivide the equatorial Pacific into rectangular grid boxes surrounding each mooring site with east–west boundaries equidistant from the mooring-line longitudes and north–south boundaries equidistant from the mooring latitudes. These buoy boxes are filled with the wind stress anomalies estimated from the mooring wind observations when the mooring winds are available. Zero anomaly (i.e., climatological wind stress) is applied in this case when the moored-buoy wind observations are unavailable. We refer

to this wind stress field as TAO_{box} hereinafter. We also use a second TAO-based approach in which the gaps caused by buoy dropouts are filled using linear interpolation when observations from adjacent buoys are available. We refer to this x - and y -direction-interpolated case as TAO_{xyf} .

Wind speed and direction information over the equatorial Pacific was also acquired on the basis of a pair of satellite-based scatterometers (QuikSCAT and ASCAT-A), which offer surface-roughness (backscatter)-based wind estimates. Together, QuikSCAT and ASCAT-A span the calendar years from 2000 to the present (QuikSCAT ended in 2009; ASCAT-A started in 2007 and remains operational as of the preparation of this paper). The scatterometer data used here are produced by the Remote Sensing Systems Co., sponsored by the NASA Ocean Vector Winds Science Team, and processed using the C-2015 model function (Ricciardulli and Wentz 2016) for ASCAT and the Ku-2011 model function (Ricciardulli and Wentz 2015) for QuikSCAT. These scatterometer wind model functions were designed to yield wind speed and direction information at 10-m height that are consistent across the two different instruments and on a 0.25° grid. Both scatterometers measure winds along the equatorial Pacific in a series of daily ascending (traversing the surface in a nearly south-to-north path) and descending (north to south) satellite passes, approximately six of which occur per day over the equatorial Pacific. The ~ 1600 -km-wide QuikSCAT swaths typically combine to provide at least one measurement per day in the 0.25° grid boxes spanning the equatorial Pacific, except when rain is present. The scatterometer winds are converted to wind stress using the equation above. Each day's ascending and descending passes are averaged in the case that overlap occurs. The ASCAT-A data are treated similarly to the QuikSCAT data herein. The ASCAT-A antennae geometry, however, is different from QuikSCAT's to the effect that each ASCAT-A pass provides two ~ 500 -km-wide swaths of measurements separated by a 360-km gap in the east–west direction. Daily ASCAT-A coverage along the equatorial Pacific is less than QuikSCAT's, typically only around 60%–65%. Application of 3-day averaging, applied here using a 1–2–1-day triangle filter, fills most of these gaps, leaving the 3-day averaged ASCAT-A record $\sim 90\%$ complete along the Pacific Ocean waveguide. This 3-day averaging is also applied to the QuikSCAT record. QuikSCAT data were used in their entirety over the period for which they were available, and ASCAT-A data were used thereafter. At the time of paper preparation, the delay for ASCAT-A data is ~ 2 weeks. Ways to decrease this delay are under investigation (L. Ricciardulli 2018, personal communication). We refer to the QuikSCAT + ASCAT-A wind stress field as “SCAT.”

We construct and examine a third wind stress anomaly dataset in which the TAO_{box} observations are used when and where they are available, and the buoy-dropout gaps are filled with the SCAT wind stress field. We refer to this case as TAO_{SCAT} .

We also use surface wind stress estimates from the NCEP–NCAR Reanalysis-1 (NCEP1 1996) described by Kalnay et al. (1996). NCEP-1 is a numerical weather model run in data assimilation mode. NCEP-1 assimilates the TAO/TRITON observations and is provided at 2.5° and 6-hourly resolution. NCEP-1 wind stress analyses are typically available with only 1 or 2 days lag. Time–longitude 5°S – 5°N averaged wind stress estimates during 2017 from NCEP-1, ASCAT-A, TAO_{SCAT} , TAO_{xyf} , and TAO_{box} are provided in Fig. S1 of the online supplementary material.

The ocean general circulation model used here is based on NOAA GFDL's MOM, version 4.1 (MOM4; Griffies et al. 2003). It is employed with 27 vertical levels consisting of a uniform 10 m grid in the upper 100 m, upper grid point at 5 m, and gradually decreasing vertical resolution below 100 m. The horizontal grid is uniform between 10°N and 10°S , with 0.33° resolution in latitude and 1.0° resolution in longitude. Poleward of 10° the meridional resolution increases nonuniformly to 50°N and to 25°S . The model is spun up over 30 years by applying the climatological wind stress developed from the COADS marine dataset and Large and Pond (1981) stability dependent drag coefficient by Harrison (1989) and surface heat flux parameterization of Harrison et al. (2009), which utilizes the shortwave parameterization in terms of model SST of Harrison (1991) and sets longwave flux to 55 W m^{-2} . Run in this climatological mode, this model rather accurately reproduces the main features of the observed climatological upper ocean currents and thermal structure, including the zonal gradient in equatorial SST. Climatological-mode simulations from this model were used by Harrison et al. (2009) to examine the role that the different components of surface forcing, including zonal and meridional stress, play in driving these observed features of the upper Pacific Ocean's mean seasonal cycle.

In the experiment mode, the longwave and shortwave fluxes are specified as in the spinup, but latent and sensible heat fluxes are determined differently, based on the applied wind speed calculated from the applied wind stress, and a constant sea surface to 2-m air temperature difference of 1°C and constant near-surface relative humidity of 0.8. These constants are broadly representative of the average conditions over tropical oceans and were also used by Philander and Siegel (1985). A salient feature of this parameterization is that the model is not constrained by observed air temperature, observed near-surface humidity or surface temperature in experiment mode, and is thus free to simulate inaccurate SSTAs if forced with inaccurate wind stress.

SSTAs are simulated here as the difference between a control run, forced with the climatological wind stress used in the spinup and an experiment run that is the same as the control except that zonal wind stress anomaly from one of the candidate datasets (TAO_{box} , TAO_{xyf} , TAO_{SCAT} , SCAT, NCEP-1) is added to the climatological zonal stress. The experiment runs begin from climatological ocean initial conditions (hence, zero initial ocean anomaly) on 1 January of the given year. The experiment runs are forced for 1 year. So, in order to compare observed and simulated end-of-year Niño-3.4 conditions over the 1992–2017 period, a series of 26 yearlong integrations was performed for each wind stress dataset.

The effects of using slightly different model experiment start dates (e.g., 1, 3, 6, or 9 January) was tested and found to cause only very small changes in the simulated Niño-3.4 SSTA trajectories [e.g., monthly Niño-3.4 root-mean-square differences (RMSDs) of only $\sim 0.01^{\circ}\text{C}$ in the 2017 simulations discussed in the first figure below]. Thus, only runs starting from 1 January are discussed herein.

NOAA OISST (Reynolds et al. 2002) is used for verification of the forced-ocean model simulations. Preliminary examination (not shown) revealed that OISST Niño-3.4 trajectory was closest to that measured by TAO/TRITON near-surface ocean temperatures (5-m depth) among NOAA ERSST (v5) and Hadley Centre SST (HadISST). The agreement between TAO/TRITON SSTs, averaged over the Niño-3.4 region, and Niño-3.4 based on OISST is close enough that the TAO/TRITON result can be substituted for OISST in the 2017 simulations discussed below, and the results remain quantitatively (RMSD $< 0.02^{\circ}\text{C}$) and qualitatively similar.

Arithmetic integrals of zonal wind stress anomaly calculated on a year-by-year basis over the seasons typically associated with ENSO onset and development (e.g., from spring through fall of ENSO year 0) are also used to statistically forecast Niño-3.4 conditions at the end of the (same) calendar year in section 6. The effects of using different start dates (arithmetic integration time scales) and end dates (forecast leads) are explored. To do this, the wind stress integrals were calculated using end dates stepped one month apart. The longest lead forecast considered has 30 April as end date. The shortest lead forecast would be issuable on the last day of November. These end dates were paired with the different possible first of the month start dates that provide at least two full months of integration time, beginning with 1 March. Thus, with 30 April as the end date there is only one integration period considered (1 March–30 April). With 31 May as the end date there are two integration periods considered (1 March–31 May, 1 April–31 May), in the 30 June end date case there are three integration periods (1 March–30 June, 1 April–30 June, 1 May–30 June), and

so forth. Comparison of results that are based on the same end date but different start dates allows for the effects of the integration time span to be examined at a given forecast lead. The earliest start date evaluated herein is 1 March because preliminary examination showed that using start dates prior to 1 March only resulted in degradation of forecast skill. Closer inspection of pre-March winds (not shown) revealed that the anomalies found at the beginning of years categorizable as year +1 of some of the larger ENSO events in record (e.g., 2016 of the 2015/16 El Niño) often exhibited anomaly conditions more closely associated with the (previous) ENSO event peak than subsequent ENSO development. This at least partly explains why tabulating pre-March winds was found to be unhelpful in this context.

The core spatial wind stress measure used for integration here is the zonal stress anomaly calculated using TAO_{SCAT} and averaged between 5°S and 5°N , and 130°E and 120°W . 130°E is the western edge of our model domain, and 120°W the eastern edge of the Niño-3.4 averaging region. It is over this fetch that equatorial Pacific zonal momentum stress most efficiently drives SSTA change over the eastern central equatorial Pacific (including the Niño-3.4 region) by exciting eastward propagating equatorially trapped oceanic baroclinic Kelvin waves.

To assess forecast skill in this case, wind stress integrals over preceding seasons are used to statistically predict target December–February (DJF) Niño-3.4 values based on linear regression and leave-one-out cross validation. In the cross-validation step, the linear regression coefficients by which a given year's wind integral (predictor) is converted to DJF Niño-3.4 (prediction) were calculated using information from all years in the 2000–17 period except for the year in question. Cross-validation methods such as this are used to avoid specifying the answer to retrospective forecast methods and thereby overestimating forecast skill.

3. Simulating 2017 Niño-3.4 development

Monthly averaged Niño-3.4 SSTA exhibited near-neutral conditions through most of the first 3 months of 2017 (January through March averaged Niño-3.4 = -0.05°C). Springtime warming drove the June 2017 Niño-3.4 average to the $+0.5^{\circ}\text{C}$ level, which corresponds approximately to $+0.5$ standard deviations ($\sigma = 0.94^{\circ}\text{C}$ based on monthly averaged Niño-3.4 values from 1992 to 2017). This early 2017 warming tendency changed sign abruptly in July, however, and Niño-3.4 cooled to -0.2σ by August and ended the year with a December average of -0.9σ (Fig. 1, black curves in each panel). Despite having warmer than average midyear central Pacific SSTA conditions, 2017 reached

2017 Niño 3.4 SSTA

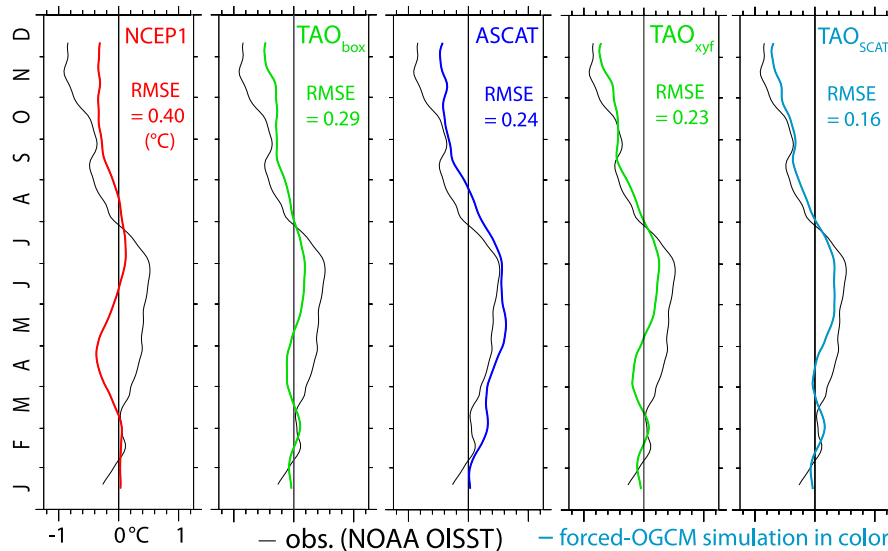


FIG. 1. Monthly-averaged Niño-3.4 SSTA in 2017 as based on the NOAA OISST observational compilation (black curves) and ocean model simulations forced by applying zonal wind stress anomalies from different datasets (colors as listed).

“La Niña” status around the end of the calendar year based on the commonly used SSTA-based definitions (e.g., NOAA’s Climate Prediction Center has traditionally defined La Niña as an interval in which 3-month-averaged Niño-3.4 $< -0.5^{\circ}\text{C}$ for five consecutive months). The 2017 October–December (OND)-averaged Niño-3.4 value was -0.75σ based on NOAA OISST (2002; Reynolds et al. 2002) and the 1992–2017 base period.

The 2017 Niño-3.4 trajectory simulated by forcing our ocean model with NCEP-1 zonal stress anomaly is not very accurate (Fig. 1, left panel). NCEP-1 wind stress drives cooling, rather than the observed warming through April and substantially weaker-than-observed cooling over the latter half of the year. The NCEP-1-forced December-averaged Niño-3.4 value is 0.6°C warmer than observed. The RMSE of the NCEP-1 simulation, calculated based on the simulated and observed trajectories of monthly averaged Niño-3.4 during 2017 is 0.40°C , nearly equal to the observed 2017 monthly averaged Niño-3.4 standard deviation of 0.45°C (σ_{17}). The signal-to-noise ratio of the NCEP-1 simulation (σ_{17}/RMSE) is thus ~ 1 .

Forcing the model with the TAO_{box} zonal stress field offers a substantially more accurate simulation than produced by forcing with NCEP-1. The TAO_{box} simulation is 28% more accurate than the NCEP-1 result based on their respective RMSEs of 0.29° and 0.40°C . The TAO_{box} simulation is still less than satisfying, however. For example, TAO_{box} simulated Niño-3.4 warms insufficiently during the first half of the year and cools insufficiently

through the second half, ending the year with a simulated December-average Niño-3.4 value that is 0.4°C warmer than observed (Fig. 1, panel second from left).

The ASCAT-A simulation (Fig. 1, center panel) has an RMSE of 0.24°C and thereby achieves a signal-to-noise ratio of ~ 2 . The ASCAT-A simulation, however, still ends the year with its December-averaged Niño-3.4 value approximately 0.4°C warmer than observed.

Inspection of the daily averaged mooring and scatterometer wind stresses from mid-February reveals that a westerly wind event with duration (~ 1 week), amplitude (>0.045 Pa), and zonal length scale (~ 2000 km) broadly consistent with the westerly event composite average (e.g., Vecchi and Harrison 2000) occurred in a hole in the mooring array caused by the loss of most of the buoys in the far western equatorial Pacific (Fig. 2, upper two panels). An interestingly comparable situation occurred in September 2017, when an EWS occurred with its equatorial peak in zonal stress anomaly located in a hole caused by the loss of some central equatorial Pacific buoys (Fig. 2, lower two panels). These types of occurrences (wind events in buoy-dropout gaps) largely explain the differences between the 2017 TAO_{box} simulation, which failed to warm as much as observed following the missed westerly and cool as much as observed following the missed easterly wind event, and the TAO_{xyf} and TAO_{SCAT} results, which tracked the observed SSTA development better than TAO_{box} .

The TAO_{xyf} run (Fig. 1, second panel from right) produces an RMSE of 0.23°C and further improves upon

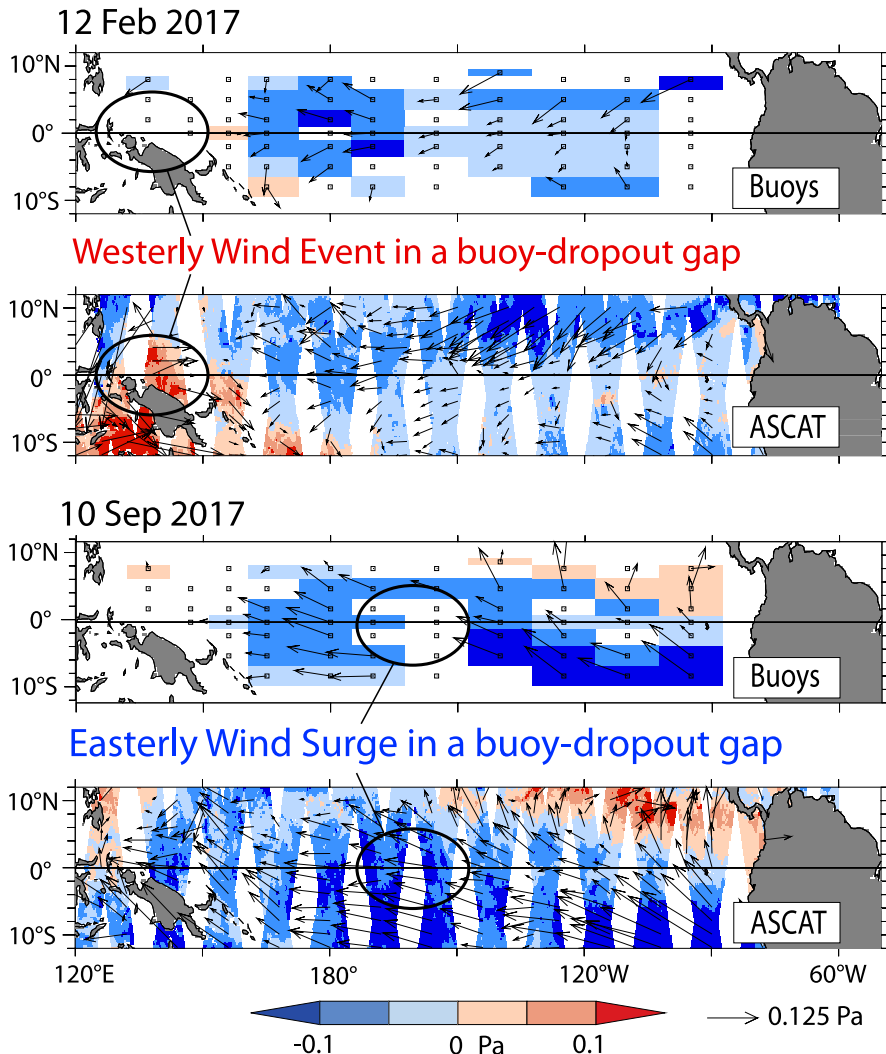


FIG. 2. Daily averaged snapshots of wind stress information available on 12 Feb and 10 Sep 2017 from the tropical Pacific moored-buoy array and the satellite-based ASCAT-A scatterometer. The wind events depicted last longer than a day; snapshots are offered here to illustrate data return from these two platforms (satellite and moored-buoy array).

the ASCAT-A result by ending the year with December-averaged Niño-3.4 much closer to the observed value (within 0.2°C of observations). Forcing the model with the TAO_{SCAT} field (Fig. 1, right panel) produces a simulation that achieves RMSE of 0.16°C. This represents a factor 2 improvement in RMSE over the NCEP-1 result. The signal-to-noise ratio ($\sigma_{17}/RMSE$) of the TAO_{SCAT} simulation is ~ 3 .

If the period over which the RMSE is calculated is changed from starting in January to starting in July, so that the period over which the model first develops SSTA (e.g., the first few months of 2017) and the effects of (the array missing the) early year western Pacific westerly wind event activity are minimized, then the signal-to-noise ratio

of TAO_{xyf} (3.25) improves to the level of TAO_{SCAT} (also 3.25 over July–December). The signal-to-noise ratio of the other runs remain relatively unchanged in this case (e.g., NCEP-1 signal to noise over July–December is ~ 1). This supports the conclusion that the moored-buoy array works well when operating as designed and satellite winds are mainly useful in this context when large portions of the moored-buoy array are unavailable.

In summary, on the basis of 2017 Niño-3.4 simulations, comparison of the TAO_{SCAT} and TAO_{xyf} results highlighted the need to patch the gap in the moored-buoy array caused by the TRITON part of the array (12 sites along 137°E, 147° and 156°E) being reduced to two moored buoys. Even so, TAO_{xyf} performed about as well

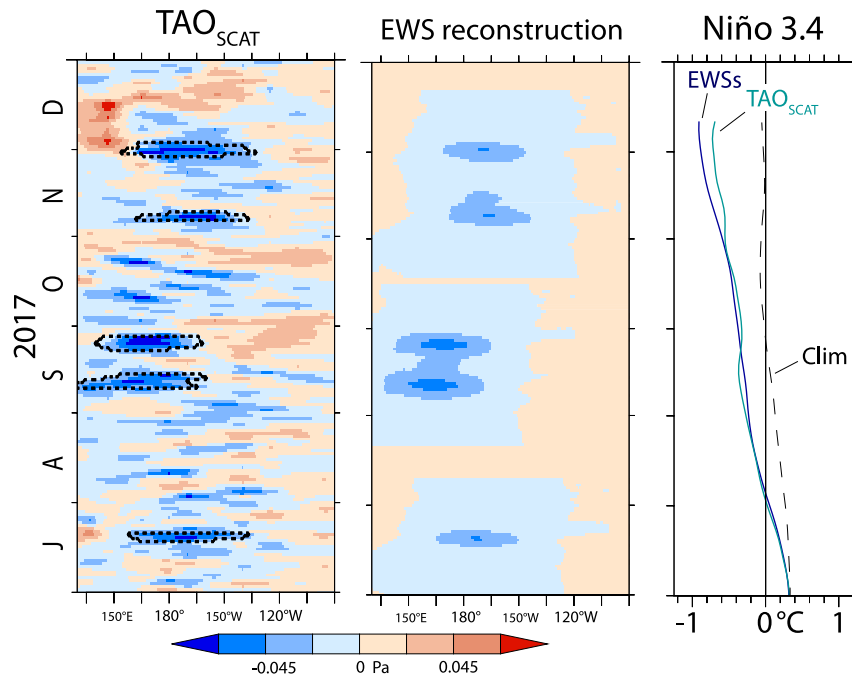


FIG. 3. (left) The 5°S–5°N averaged zonal wind stress anomaly over the equatorial Pacific during 2017 based on mooring plus scatterometer (TAO_{SCAT}) winds. Dashed black curves circumscribe the identified wind events in this period. (center) Zonal wind stress anomaly reconstructed by applying five composite-average EWS zonal wind stress anomalies at the times and longitudes of the observed events. (right) Niño-3.4 simulated by forcing the ocean model over the period shown with these two zonal wind stress fields as well as climatological zonal wind stress (dashed line).

as TAO_{SCAT} . Both TAO_{SCAT} and TAO_{xyf} simulations end the year with accurate Niño-3.4 conditions. NCEP-1 produced a substantially higher level of error than the other four wind stress fields considered.

4. The role of easterly wind surges in driving the 2017 La Niña

Successful simulation of the observed 2017 Niño-3.4 development trajectory provides grounds for understanding that development based on characteristics of the applied wind stress variability. Closer examination of the 2017 TAO_{SCAT} field reveals that the equatorial easterly wind stress anomalies responsible for the development of La Niña-type SSTAs during late boreal summer and fall are concentrated in synoptic-scale easterly wind events: Application of the wind event detection algorithm described by Chiodi and Harrison (2015a) identifies a series of five EWSs during the second half of 2017, beginning with an event centered near 170°W in July, followed by a pair of EWSs centered around 165°E in September and subsequent central-basin events in October and November (Fig. 3, left panel). No large westerly wind events were observed during this period.

To examine the effects of this wind event distribution on model SSTA development, the post-June 2017 TAO_{SCAT} zonal stress anomaly field was reconstructed by applying five averaged-size (Chiodi and Harrison 2015a) EWS wind stress anomaly composites at the locations and times of the observed surges. Experiment reveals that forcing the model with TAO_{SCAT} stress through June 2017 and then the five EWSs from July through December 2017 drives Niño-3.4 development that closely tracks the TAO_{SCAT} result (Fig. 3, right panel). The EWSs run also ends with an accurate Niño-3.4 value (December model average Niño-3.4 within 0.04°C of OISST). If none of these five EWSs are applied over the second half of 2017, model-simulated Niño-3.4 quickly returns to and stays in near-neutral conditions (0°C) over this period (Fig. 3, dashed curve). In this forced-ocean context, the unexpected midyear reversal in 2017 Niño-3.4 development was driven by a series of EWSs distributed over the second half of 2017.

5. Simulating end-of-year Niño-3.4 conditions, 1992–2017

The 2017 results suggest that TAO_{xyf} , or TAO_{SCAT} in the case in which many buoys are missing, provides more

TABLE 1. RMSE between observed and forced-ocean-model-simulated OND-averaged Niño-3.4 conditions.

Wind stress forcing data	OND Niño-3.4 RMSE 1992–2017 (°C)	OND Niño-3.4 RMSE 2000–17 (°C)
TAO _{SCAT}	—	0.43
TAO _{xyf}	0.44	0.44
TAO _{box}	0.49	0.50
SCAT	—	0.51
NCEP-1	0.68	0.65

accurate winds for simulating ENSO SSTA development than the other options considered. But how well do these results apply to other years? To evaluate the extent to which the 2017-based ranking of simulation accuracies hold over all years in the study period, a corresponding series of yearlong experiments was run using each wind stress dataset and beginning in 1992 in the TAO_{box}, TAO_{xyf}, and NCEP-1 cases and 2000 in the SCAT and TAO_{SCAT} cases.

Comparison of simulated and observed end-of-year (OND) Niño-3.4 SSTA conditions reveals that NCEP-1 RMSE (0.68°C) is 60% as large as the magnitude of the signal in question (observed Niño-3.4 OND standard deviation is 1.1°C). Forcing with SCAT or TAO_{box} offers substantial improvement over the NCEP-1 results, with RMSE about one-half of the observed OND Niño-3.4 standard deviation (Table 1). And further improvement was achieved by filling the TAO_{box} lost-buoy gaps with either the scatterometer measurements (TAO_{SCAT}; 2000–17 RMSE = 0.43°C), or by interpolation from adjacent buoys (TAO_{xyf} 1992–2017 RMSE = 0.44°C, 2000–17 RMSE = 0.44°C). Thus, the 2017 case example is broadly consistent with results aggregated over the last two decades: using TAO_{xyf} or TAO_{SCAT} consistently offers improved simulation accuracy over the other cases, especially NCEP-1.

Inspection of the TAO_{xyf} simulated and observed OND Niño-3.4 values (Fig. 4; period 1992–2017) reveals that when the model is incorrect, it tends to be because the simulated amplitude is smaller, rather than larger than observed. Nonetheless, some moderate-to-strong ENSO events are reasonably well reproduced (e.g., 2002–03, 2007–08, and 2015–16). Determining why some moderate-to-large events are and are not (e.g., 2009–10) adequately simulated is difficult with the information available presently. Effects of omitted initial ocean conditions, errors in the ocean model or the applied surface heat fluxes, and errors in the winds are all possibilities. Without a more complete and accurate knowledge of the wind stress than is currently available it is difficult to say which is more likely: even in the best-sampled years, TAO/TRITON data return has not

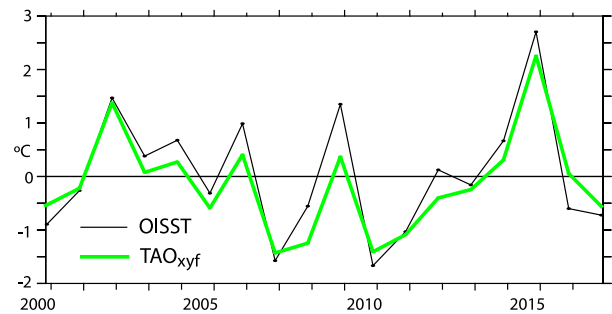


FIG. 4. OND-averaged Niño-3.4 as based on OISST (black curve) and as simulated in the TAO_{xyf} (green) forced-ocean general circulation model experiment.

much exceeded 80%, leaving open the possibility that impactful wind variability was not directly observed by the moored-buoy array.

QuikSCAT wind measurements are not available after 2009, whereas ASCAT-A began in 2007 and remains operational. The TAO_{xyf} results span this full satellite era (2000–17) and therefore offer a useful benchmark for comparing these two scatterometers in terms of simulation accuracy. Looking over the QuikSCAT period, very little difference in accuracy is found between the QuikSCAT and TAO_{xyf} simulations: 2000–09 OND Niño-3.4 RMSE is 0.48°C in the TAO_{xyf} case and 0.48°C in the QuikSCAT case. A larger discrepancy is revealed, however, by comparing TAO_{xyf} and ASCAT-A results over the 2007–17 period. In this case, OND Niño RMSE based on TAO_{xyf} remains about as accurate (within 2%) as in the 2000–09 case (2007–17 TAO_{xyf} RMSE = 0.49°C), but 2007–17 RMSE is 0.60°C in the ASCAT-A case. Evidently, ASCAT-A is not QuikSCAT's or TAO/TRITON's equal in its ability to provide the basinwide wind knowledge needed to accurately simulate observed end-of-year Niño-3.4 conditions.

6. Predicting DJF Niño-3.4 SSTA from zonal wind stress integrals

The results described above demonstrate that the zonal wind stress applied each year over the equatorial Pacific waveguide provides a dominant control on the development of that year's end-of-year Niño-3.4 SSTA conditions. They also demonstrate that accurately simulating that development in the free-forced-ocean model requires accurate wind knowledge. Further, not all popular sources of wind information are accurate enough to do this.

Skillful forecasts of ENSO anomaly state can provide a useful basis for issuing seasonal weather forecasts over the strongly ENSO-affected regions worldwide. Skill in predicting Niño-3.4 is often used as a benchmark within the larger-scale prediction process. We now examine how

well Niño-3.4 conditions in boreal winter (when ENSO events tend to peak and have strongest statistical linkages to extratropical seasonal weather anomalies) can be predicted based on accurate knowledge of winds in the preceding seasons.

To do this, the best-performing TAO_{SCAT} zonal wind stress is arithmetically integrated (no ocean modeling is used in this section) on a yearly basis and over the boreal spring through fall, the seasons typically associated with ENSO event onset and development (Larkin and Harrison 2002). The target wintertime (DJF) Niño-3.4 averaging period will remain constant in this examination. Thus, stepping the integration end date back in time from, say, 30 November to 31 October or 30 September, equates to increasing forecast lead. Different wind-integral start dates, back to 1 March, are used to explore the effects of changing the integration period within the traditional ENSO onset and development seasons.

The results of integrating equatorial Pacific zonal wind stress anomaly from 1 May through 31 October of each year for which TAO_{SCAT} data are available (2000–17) are illustrated in Fig. 5. In this case, there is 1 month of lead time between the end of the integration period and start of the target (DJF) period. The stress integral correlates at the 0.94 level with observed DJF Niño-3.4 in this case. By the traditional method for estimating variance explained on the basis of the squared correlation coefficient, equatorial Pacific wind stress integrated over the boreal spring–fall accounts for 89% of the observed DJF Niño-3.4 variance.

Recalculating this integral again over the same 1 May–31 October period, but this time tabulating only the times and longitudes identified by the wind event detection algorithm (e.g., regions denoted by the black-dashed curves in the left panel of Fig. 3) very nearly reproduces the forecast skill achieved using the total zonal wind stress field: Integrating just over the wind events produces a correlation coefficient with DJF Niño-3.4 (0.89) that is within 5% of the result based on integrating over the total TAO_{SCAT} field. This, along with the EWS-reconstruction results described in section 4, strongly suggests that learning to accurately predict the distribution of wind events in a given year, or at least some salient aspects of their distribution (e.g., whether or not events of one sign will be strongly favored over the other) would offer direct improvement to our ability to forecast wintertime ENSO SSTA conditions. The forecast benefits associated with learning to better anticipate westerly wind event activity have also previously been examined and found to be substantial by Lopez and Kirtman (2014), who determined this based on experiments with adding westerly wind events, whose

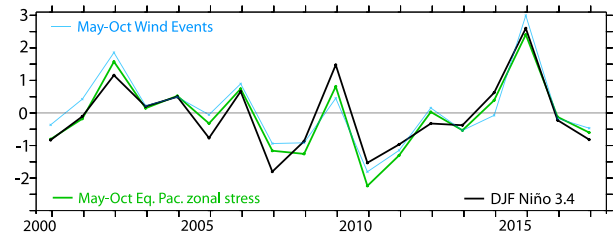


FIG. 5. DJF-averaged Niño-3.4 ($^{\circ}\text{C}$; black curve) and equatorial Pacific zonal wind stress anomaly integrated from 1 May through the end of October of each year (green curve). The wind integral is plotted with equivalent standard deviation. The X -axis values correspond to the year over which the stress was integrated and the corresponding first month (December) of the DJF Niño-3.4 average. The blue curve shows the result of integrating just over the times and longitudes of the identified easterly and westerly wind events.

frequency is linked to equatorial Pacific SSTAs, to coupled atmosphere–ocean general circulation model experiments.

Further experimentation reveals that using a higher wind stress anomaly threshold (specifically 0.0675 Pa, which is an increase of 50% over the original 0.045-Pa criterion) for wind event detection results in a very similar anomaly correlation as before (0.87) but a change in the character of the predicted DJF Niño-3.4 time series (not shown) such that the larger ENSO event years (e.g., 2010–11, 2011–12, and 2015–16) stand out more from the other years. This change in character causes an increase in the kurtosis of the predicted DJF Niño-3.4 time series (period 2000–17) from 4.5 to 7.4. This may imply that focusing on strong wind event behavior will help distinguish (prior to winter) the major ENSO events that are most likely to influence extratropical wintertime weather conditions. Further examination of this possibility is left to future work.

The left panel of Fig. 6 illustrates how well the wind stress integral correlates with DJF Niño-3.4 at different integral end dates and the same start date of 1 March (effects of changing start dates examined below). The wind stress–integral anomaly correlation increases from just above 0.6 in the April-end case, to approximately 0.95 in the October-end and November-end cases (Fig. 5 left panel)

SSTA persistence (autocorrelation) has traditionally been a useful point of comparison for other strategies for forecasting Niño-3.4 (Barnston et al. 2012). The results of performing such a comparison in the present context are illustrated in the right panel of Fig. 5, wherein the anomaly correlation values shown in the left panel are replotted after the corresponding SSTA-persistence correlations have been subtracted. In this case, the SSTA-persistence anomaly correlations (with DJF Niño-3.4) are

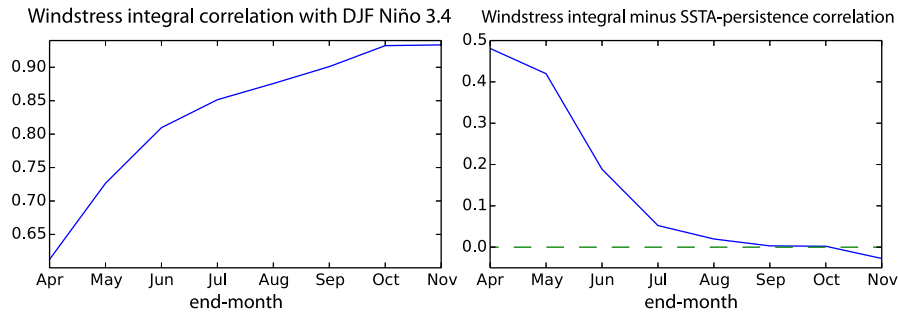


FIG. 6. (left) Correlation between DJF Niño-3.4 and zonal stress integrals starting 1 Mar of each year and running through the month shown on the x axis. (right) Result of subtracting corresponding 3-month-averaged Niño-3.4 time-lagged autocorrelations from the stress integral results shown in the left-panel. The corresponding Niño-3.4 lagged autocorrelations in this case are calculated using the target DJF Niño-3.4 average and the Niño-3.4 average over the three consecutive months ending with the month shown on the x axis.

calculated from 3-month averages of Niño-3.4 with the same end date as the given wind stress integral. For example, the 1 August–31 October-averaged (ASO) SSTA-persistence anomaly correlation (~ 0.94) is subtracted from the 31 October end date wind stress-integral result (correlation ~ 0.95) to determine which approach offered a closer statistical link to DJF Niño-3.4 conditions. Evidently, the wind-integral anomaly correlation fails to reach the SSTA-persistence benchmark at the shortest lead considered (November end), rises (barely) above this benchmark when lead time is increased by 1 month, and then beats the SSTA-autocorrelation benchmark by increasingly wider margins as lead time is increased. Specifically, springtime wind stress integrals produce correlations with DJF Niño-3.4 that are 0.4–0.5 higher than those based on SSTA persistence. This highlights the potential long-lead (4–8 months) predictive utility offered from accurately monitoring and tabulating wind stress variability over the equatorial Pacific.

The variation of the wind stress-integral anomaly correlation with changes integration interval (i.e., using different integral start dates) was examined. Results reveal that all the integration periods considered that extend through September or later produce correlations with DJF Niño-3.4 that are >0.9 (Fig. 7, left panel). The subset of late summer and early fall end date results are slightly improved when the integration starts in June or July rather than March or April, but otherwise the variation with start date is generally smaller than the effects of changing the end date (lead time).

Retrospective statistical forecasts of DJF Niño-3.4 were produced based on the set of spring through summer and fall wind stress integrals illustrated in Fig. 6 using linear regression with the target (observed DJF Niño-3.4) and leave-one-out cross validation. The RMSE of the cross-validated set of wind-based forecasts

of DJF Niño-3.4 (Fig. 7, right panel) varies with integration interval in a manner akin to that of the corresponding anomaly correlation; better skill is generally (and perhaps unsurprisingly) seen the closer the integral end date is moved to the start of the target DJF period. The standard deviation of DJF Niño-3.4 over the 2000–17 period is 1.1°C . Dividing this standard deviation by a given forecast's RMSE offers a useful measure of that forecast's signal-to-noise ratio. Forecasts achieving signal-to-noise ratios ≥ 2 are available as early as June, in which case the 1 May–30 June integration period performs best. Forecasts based on integrals ending in August or later achieve this same level of accuracy (signal-to-noise ≥ 2) regardless of the start date that is chosen.

A benchmark set of predictions based on SSTA persistence (i.e., time-lagged autocorrelation of 3-month-averaged Niño-3.4) was generated using the same linear regression and leave-one-out validation method as in the wind stress-integral case. Comparison reveals that the wind-integral method beats persistence method for all lead times (end dates) considered, with the exception of the shortest (the November end date). The utility of using wind as predictor for DJF Niño-3.4 is thus confirmed at leads longer than 1 month relative to the SSTA-persistence basis.

But how well does this wind-based Niño-3.4 forecasting approach work compared to the coupled ocean-atmosphere model forecast systems in current popular use? The NOAA CFSv2 (Saha et al. 2010) has been found, in terms of Niño-3.4 forecast skill, to be among the top, if not the top-performing model contributing to the North American Multi-Model Ensemble (NMME; Kirtman et al. 2014). RMSEs calculated from CFSv2 ensemble-averaged forecasts of DJF Niño-3.4 (2000–17) are plotted as a function of lead time in Fig. 8, with the

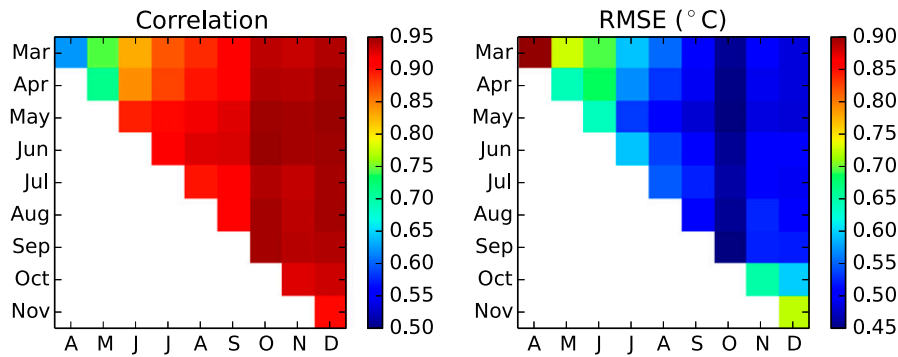


FIG. 7. (left) Correlation coefficient between DJF-averaged Niño-3.4 and integrated equatorial Pacific wind stress anomaly. The end date (last day of month listed) is given on the x axis and start date (first day of month) is on the y axis. (right) RMSE between observed DJF-averaged Niño-3.4 and Niño-3.4 values predicted by the wind stress–integral linear-regression model, with leave-one-out cross validation applied.

corresponding wind stress–integral results overlaid for comparison. At the two longest leads considered (April and May end dates) CFSv2 RMSE is lower (better) than the wind stress–integral results. At these longer leads, however, RMSEs are near the target standard deviation indicating that very reliable long-lead forecasts are not available by either approach. CFSv2 skill also beats the wind approach result at the shortest (November end) lead considered, however, the Niño-3.4 autocorrelation method beats both wind and CFSv2 results in this case (September–November Niño-3.4 autocorrelation-based prediction of DJF Niño-3.4 yields RMSE = 0.24°C). Over the summer and fall end date cases that offer signal-to-noise ratios > 2 , the wind-integral approach achieves forecast skill that is either very near or improves upon that achieved by CFSv2. In other words, over the times of year when it was most useful to look at the coupled model system forecasts of Niño-3.4, the

benefit of doing so could have been easily replicated, if not improved upon, by looking at the winds made available from the tropical Pacific mooring array—with gaps caused by the (episodic) loss of an unusually large number of buoys filled by the right kind of scatterometer wind information.

7. Discussion and conclusions

The tropical Pacific moored-buoy array remains a critical component of the Tropical Pacific Observing System for its ability to provide direct, high-quality, real-time observational knowledge of waveguide-wide wind variability associated with the development of El Niño and La Niña events. Most ENSO studies, however, do not use the mooring winds directly for wind or wind stress information, and instead rely on reanalysis data products like NCEP-1. Of the reanalysis wind products

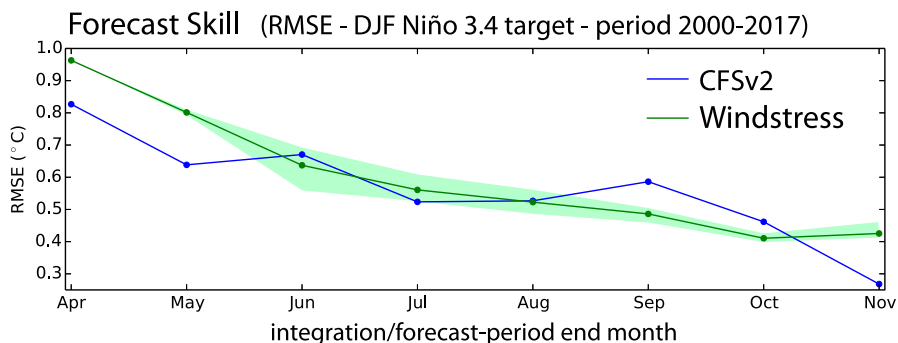


FIG. 8. RMSE of wind stress integral–based (green curve; using TAO_{SCAT} data) and CFSv2–based forecasts of DJF Niño-3.4 SSTA. In the wind stress case, green shading shows the range available from using different integration start dates (but the same end date) and the solid line illustrates the average. The integration end dates and forecast dates are the last day of the months listed on the x axis.

most commonly used in recent ENSO studies (e.g., NCEP-1, NCEP–DOE Reanalysis-2, ERA-Interim; cf. Chiodi and Harrison 2017a) only NCEP-1 is available in near–real time, which motivates its direct consideration herein.

Although NCEP-1 has proven remarkably useful for understanding SSTA developments in other situations, including those caused by subtropical air–sea interaction (Chiodi and Harrison 2006, 2007), results from our forced-ocean model experiments show it to be a deficient source of wind stress knowledge for simulating the observed development of equatorial Pacific SSTA development in 2017 (signal-to-noise-ratio ~ 1). Synthesizing a waveguide-wide wind stress field from the buoy winds on their own offers a substantially improved basis for understanding 2017 Niño-3.4 development (signal-to-noise ratio = 2–3).

These results are consistent with those based on other years, such as were described over the 1992–2011 period by Chiodi and Harrison (2017a), who showed that the winds from the mooring array, when operating as designed, provides basis for adequately simulating (RMSE $< 1/2$ of the target standard deviation) observed end-of-year Niño-3.4 conditions. Previous results also showed that there are deficiencies in each of the reanalysis product winds that prevent them from achieving the simulation accuracy provided by the moorings. Specifically, the NCEP reanalysis wind products tend to contain less variability than observed across a wide range of time scales. Corresponding NCEP-forced simulations tend to produce lower-than-observed Niño-3.4 variability. Over the 1992–2017 period considered herein, the NCEP-1-forced simulations yielded OND averaged Niño-3.4 values with a standard deviation of 0.6°C , which is 0.5°C less than the observation-based OISST value of 1.1°C . Also, the ERA-Interim product was previously found to contain a spurious easterly trend component over the equatorial Pacific that degraded its simulation accuracy. A similarly spurious (relative to the mooring winds) decadal-scale increase in zonal wind speeds was also recently found over the tropical Pacific in the satellite-wind-focused Cross-Calibrated Multi-Platform, version 2, wind product (CCMP2; Atlas et al. 2011; Chiodi et al. 2019), which degrades its ability to force accurate simulations of equatorial Pacific SSTA development in the model.

The efficacy of the mooring array is conditional on there being not too many large gaps in it caused by the loss of groups of adjacent buoys. Unfortunately, the array suffered such significant losses in the 2012–14 period (50% return relative to 1992–2011; Chiodi and Harrison 2017b) and is currently severely depleted in the far western Pacific. Filling such gaps with the analysis

products mentioned above only degrades the simulations. Thus, what remained unclear from previous work was whether the wind knowledge gaps caused by adjacent buoy dropouts could be filled with other sources of wind information and our knowledge of ENSO-related wind stress variability improved.

Nature provided a useful basis for examining the prospects for this in 2017 by placing westerly and easterly wind events in some holes created in the mooring array by adjacent buoy dropouts. When westerly wind events occur over the Pacific Oceanic waveguide in ENSO-neutral conditions like those seen in early 2017, they drive SSTA warming over the oceanic waveguide that averages a few tenths of a degree Celsius per event (Vecchi and Harrison 2000) and persists for 2–3 months following the end of the wind event (Kindle and Phoebus 1995; Vecchi and Harrison 2000; Belamari et al. 2003; Chiodi et al. 2014). Thus, the gap loss of early 2017 westerly wind events in the western part of the basin contributed cool bias in the buoy-forced simulation (TAO_{box}) over the following seasons. That the buoy losses in the western part of the basin were larger than can be compensated for by the minimal redundancy built into the array (loss of one buoy mitigated by observations provided by adjacent ones) explains why cross-dropout interpolation does not offer much improvement over the first half of 2017 and, hence, why TAO_{xyf} and TAO_{box} runs are similarly cool biased through mid-2017. Fortunately, in this case the ASCAT-A measurements provided measurements of the early 2017 westerly wind event zonal stress anomalies that, when used to fill the dropout gaps in the TAO_{SCAT} case, improve upon the simulations forced by the mooring winds on their own over the summer of 2017.

The September EWS offers an interesting point of comparison to the earlier westerly case. EWSs, on average, drive SSTA cooling over the waveguide akin to the warming driven by westerly wind events. The loss of several central Pacific buoys during easterly surges in the fall explains why TAO_{box} Niño-3.4 fails to cool over fall and winter as rapidly as observed. In this case, however, functioning buoys bracketed most of lost central-Pacific buoys and therefore interpolation in the TAO_{xyf} case mitigates these losses. Thus, scatterometer data offer little improvement in this case, and over the second half of 2017 (July–December) TAO_{xyf} and TAO_{SCAT} signal-to-noise ratios are both relatively good (3.25) and end-of-year TAO_{xyf} accuracy is approximately as good as TAO_{SCAT} .

The results described herein from joint consideration of moored-buoy and scatterometer winds are encouraging in that they demonstrate a near-real-time basis for forced-ocean simulation of observed Niño-3.4 development over

the last 20 years that is more accurate than that produced from the reanalysis wind datasets tried previously (NCEP-1, NCEP-DOE Reanalysis-2, ERA-Interim, and CCMP2). This offers improved basis for studying the role that near-surface wind and wind stress variability has played in the development of El Niño and La Niña events observed since 2000 for the joint-consideration case, and since 1992 based on the moorings on their own. Closer examination of the ocean processes responsible for the SSTA changes observed to follow EWSs, based on ocean model simulations forced with appropriate combinations of moored-buoy and scatterometer wind information (as described herein), may provide fertile ground for future study (cf. Giese and Harrison 1991; DiNezio et al. 2009).

Although the currently available ASCAT-A winds provide a useful backup for major moored-buoy losses, they do not offer equal simulation accuracy to that provided by the buoys. ASCAT-A simulation accuracy, based on end-of-year Niño-3.4 RMSE, is 23% less than that provided by the mooring winds on their own over the subset of years (2007–17) for which both sources have been available. This discrepancy occurs even though the mooring array was severely depleted in several of these years, including 2012–14, and is severely depleted at present in the far western Pacific (only two of the former 12 TRITON buoys are currently operational). These results suggest that reestablishing the traditionally, but currently unavailable far western Pacific moorings, should be a high priority for the current Tropical Pacific Observing System 2020 (TPOS 2020; Cravatte et al. 2016) effort. Even in the best-sampled years, the data return from the moored-buoy array was less than perfect (~80%). This, combined with the evident loss of signal when buoys are replaced by ASCAT-A type measurements, suggests that further improvements could be obtained if the array were developed to be more resilient to lost buoys by increasing buoy density in key regions or reengineering the buoys and their instrumentation for improved longevity. The recently released second TPOS 2020 report (Kessler et al. 2019) recommends removing most of the moored buoys on the 5° and 8° latitude lines in favor of extending some (e.g., 4 or 5) of the north–south moored-buoy lines to >10° latitude from the equator. Where the 5° and 8° moored buoys are removed, maintaining the continuity of the observations provided by the remaining 2°S–2°N moored buoys will be especially critical to our ability to monitor ENSO-related wind stress variability over the Pacific Ocean waveguide.

ENSO has gained notoriety outside of the scientific literature due to its linkages with seasonal weather anomalies in affected regions and seasons around Earth. Linkages to North American weather anomalies are

strongest in winter. The ability to statistically forecast boreal wintertime Niño-3.4 conditions based on arithmetic wind stress integrals over the Pacific Ocean waveguide during preceding seasons was examined using a straightforward, cross-validated, linear regression model over the period for which wind measurements from both Tropical Pacific mooring array and either the QuikSCAT or ASCAT-A scatterometer instruments have been available. Issued based on wind information available from 1 to 6 months before the start of the target winter-time season, retrospective Niño-3.4 forecasts based on winds achieved skill that was as good as, or better than, that offered by state-of-the-art coupled ocean–atmosphere model forecast systems (e.g., CFSv2). At longer leads, CFSv2 improves upon the wind results; however, RMSE then approaches the target standard deviation. Thus, over the times of year when ENSO SSTA forecasts are most useful, the forecast skill available from coupled model systems and statistical forecasts based on accurate knowledge of the winds are about the same.

Xue et al. (2017) have recently shown that the quality of the ocean reanalyses used to provide initial ocean conditions in coupled seasonal forecast models is dependent on there being sufficient high-quality ocean profile data to constrain them; the recent loss of most of the TAO/TRITON array over the 2012–14 was associated with a substantial increase in ocean reanalysis uncertainty. In addition to ocean observational constraints, ocean reanalyses are also influenced by an initial guess, often from an ocean model forced with wind information. Problems will occur in such a forecast system, however, if the initial guess is inaccurate (because of either the quality of wind forcing or deficiencies in the ocean model) or there is a large initial shock that occurs when the coupled model system is no longer constrained by observations in forecast mode. This suggests that successful efforts to reduce the model biases contributing to initial forecast-model shock while insuring that the winds used to initialize the ocean model are consistent with high-quality wind observations made across the entire basin (as was the objective of the original TAO/TRITON design) will improve upon our current ability to predict ENSO anomaly state with coupled atmosphere–ocean models. The results and methods presented herein will be useful for evaluating the quality of the winds used to initialize ocean reanalysis and coupled seasonal forecast models.

The real-time knowledge of equatorial Pacific wind variability provided by the tropical Pacific moored-buoy array offers critical basis for monitoring equatorial Pacific subseasonal wind events and simulating ENSO SSTA development. The other sources of wind information evaluated in this capacity, including currently

available satellite wind measurements and analyzed wind products, are less accurate than the mooring winds for these purposes. Reestablishing the mooring array in the far western equatorial Pacific is key for the continuation of our ability to monitor and improve our current understanding of the processes controlling the evolution of the anomaly state of the tropical Pacific.

Acknowledgments. This study was supported by funding from the Ocean Observing and Monitoring Division of the NOAA Climate Program Office (FundRef 100007298), NOAA's Pacific Marine Environmental Laboratory (cont. 4815) and the Joint Institute for the Study of the Atmosphere and Ocean under NOAA Cooperative Agreement NA15OAR4320063. The presentation of results benefited from helpful comments from D. E. Harrison. Directions for accessing the TAO, NCEP-1, and OISST data supporting this analysis are provided in their references. QuikSCAT and ASCAT-A data are available from Remote Sensing Systems and are described in Ricciardulli and Wentz (2015, 2016). NOAA GFDL's MOM4p1 ocean model code is available on GitHub (<https://github.com/mom-ocean/MOM4p1>).

REFERENCES

- Atlas, R., R. N. Hoffman, J. Ardizzone, S. M. Leidner, J. C. Jusem, D. K. Smith, and D. Gombos, 2011: A cross-calibrated multiplatform ocean surface wind velocity product for meteorological and oceanographic applications. *Bull. Amer. Meteor. Soc.*, **92**, 157–174, <https://doi.org/10.1175/2010BAMS2946.1>.
- Barnston, A. G., M. K. Tippett, M. L. L'Heureux, S. Li, and D. G. DeWitt, 2012: Skill of real-time seasonal ENSO model predictions during 2002–11: Is our capability increasing? *Bull. Amer. Meteor. Soc.*, **93**, 631–651, <https://doi.org/10.1175/BAMS-D-11-00111.1>.
- , —, M. Ranganathan, and M. L. L'Heureux, 2019: Deterministic skill of ENSO predictions from the North American Multimodel Ensemble. *Climate Dyn.*, **53**, 7215–7234, <https://doi.org/10.1007/s00382-017-3603-3>.
- Belamari, S., J. L. Redelsperger, and M. Pontaud, 2003: Dynamic role of a westerly wind burst in triggering an equatorial Pacific warm event. *J. Climate*, **16**, 1869–1890, [https://doi.org/10.1175/1520-0442\(2003\)016<1869:DROAWW>2.0.CO;2](https://doi.org/10.1175/1520-0442(2003)016<1869:DROAWW>2.0.CO;2).
- Chiodi, A. M., and D. E. Harrison, 2006: Summertime subtropical sea surface temperature variability. *Geophys. Res. Lett.*, **33**, L08601, <https://doi.org/10.1029/2005GL024524>.
- , and —, 2007: Mechanisms of summertime subtropical southern Indian Ocean sea surface temperature variability: On the importance of humidity anomalies and the meridional advection of water vapor. *J. Climate*, **20**, 4835–4852, <https://doi.org/10.1175/JCLI4271.1>.
- , and —, 2013: El Niño impacts on seasonal U.S. atmospheric circulation, temperature, and precipitation anomalies: The OLR-event perspective. *J. Climate*, **26**, 822–837, <https://doi.org/10.1175/JCLI-D-12-00097.1>.
- , and —, 2015a: Equatorial Pacific easterly wind surges and the onset of La Niña events. *J. Climate*, **28**, 776–792, <https://doi.org/10.1175/JCLI-D-14-00227.1>.
- , and —, 2015b: Global seasonal precipitation anomalies robustly associated with El Niño and La Niña events—An OLR perspective. *J. Climate*, **28**, 6133–6159, <https://doi.org/10.1175/JCLI-D-14-00387.1>.
- , and —, 2017a: Simulating ENSO SSTA from TAO/TRITON winds: The impacts of 20 years of buoy observations in the Pacific waveguide and comparison with reanalysis products. *J. Climate*, **30**, 1041–1059, <https://doi.org/10.1175/JCLI-D-15-0865.1>.
- , and —, 2017b: Observed El Niño SSTA development and the effects of easterly and westerly wind events in 2014/15. *J. Climate*, **30**, 1505–1519, <https://doi.org/10.1175/JCLI-D-16-0385.1>.
- , —, and G. A. Vecchi, 2014: Subseasonal atmospheric variability and El Niño waveguide warming: Observed effects of the Madden–Julian oscillation and westerly wind events. *J. Climate*, **27**, 3619–3642, <https://doi.org/10.1175/JCLI-D-13-00547.1>.
- , J. P. Dunne, and D. E. Harrison, 2019: Estimating air-sea carbon flux uncertainty over the tropical Pacific: Importance of winds and wind analysis uncertainty. *Global Biogeochem. Cycles*, **33**, 370–390, <https://doi.org/10.1029/2018GB006047>.
- Cravatte, S., and Coauthors, 2016: First report of TPOS 2020. Tropical Pacific Observing System 2020 Tech. Rep. GOOS-215, 200 pp., http://tpos2020.org/wp-content/uploads/TPOS-2020-First-Report-2018-02-14_w_errata.pdf.
- DiNezio, P. N., A. C. Clement, G. A. Vecchi, B. J. Soden, B. P. Kirtman, and S. K. Lee, 2009: Climate response of the equatorial Pacific to global warming. *J. Climate*, **22**, 4873–4892, <https://doi.org/10.1175/2009JCLI2982.1>.
- Giese, B. S., and D. E. Harrison, 1991: Eastern equatorial Pacific response to three composite westerly wind types. *J. Geophys. Res.*, **96**, 3239–3248, <https://doi.org/10.1029/90JC01861>.
- Griffies, S. M., M. J. Harrison, R. C. Pacanowski, and A. Rosati, 2003: A technical guide to MOM4. NOAA/GFDL Ocean Group Tech. Rep. 5, 342 pp., https://www.gfdl.noaa.gov/bibliography/related_files/smg0301.pdf.
- Harrison, D. E., 1989: On climatological monthly mean wind stress and wind stress curl fields over the world ocean. *J. Climate*, **2**, 57–70, [https://doi.org/10.1175/1520-0442\(1989\)002<0057:OCMMWS>2.0.CO;2](https://doi.org/10.1175/1520-0442(1989)002<0057:OCMMWS>2.0.CO;2).
- , 1991: Equatorial sea surface temperature sensitivity to net surface heat flux: Some ocean circulation model results. *J. Climate*, **4**, 539–549, [https://doi.org/10.1175/1520-0442\(1991\)004<0539:ESSTST>2.0.CO;2](https://doi.org/10.1175/1520-0442(1991)004<0539:ESSTST>2.0.CO;2).
- , and D. S. Luther, 1990: Surface winds from tropical Pacific islands—Climatological statistics. *J. Climate*, **3**, 251–271, [https://doi.org/10.1175/1520-0442\(1990\)003<0251:SWFTPI>2.0.CO;2](https://doi.org/10.1175/1520-0442(1990)003<0251:SWFTPI>2.0.CO;2).
- , A. Chiodi, and G. Vecchi, 2009: Effects of surface forcing on the seasonal cycle of the eastern equatorial Pacific. *J. Mar. Res.*, **67**, 701–729, <https://doi.org/10.1357/002224009792006179>.
- Herweijer, C., R. Seager, and E. R. Cook, 2006: North American droughts of the mid to late nineteenth century: A history, simulation and implication for Mediaeval drought. *Holocene*, **16**, 159–171, <https://doi.org/10.1191/0959683606hl917rp>.
- Kalnay, E., and Coauthors, 1996: The NCEP/NCAR 40-Year Reanalysis Project. *Bull. Amer. Meteor. Soc.*, **77**, 437–471, [https://doi.org/10.1175/1520-0477\(1996\)077<0437:TNYRP>2.0.CO;2](https://doi.org/10.1175/1520-0477(1996)077<0437:TNYRP>2.0.CO;2).
- Kessler, W.S., and Coauthors, 2019: Second report of TPOS 2020. Tropical Pacific Observing System 2020 Tech. Rep. GOOS-234, 265 pp., http://tpos2020.org/wp-content/uploads/TPOS%202020%20Second%20Report_2019May30.pdf.
- Kindle, J. C., and P. A. Phoebus, 1995: The ocean response to operational westerly wind bursts during the 1991–1992 El Niño. *J. Geophys. Res.*, **100**, 4893–4920, <https://doi.org/10.1029/94JC02392>.

- Kirtman, B. P., and Coauthors, 2014: The North American Multi-Model Ensemble (NMME): Phase-1 seasonal to interannual prediction, Phase-2 toward developing intra-seasonal prediction. *Bull. Amer. Meteor. Soc.*, **95**, 585–601, <https://doi.org/10.1175/BAMS-D-12-00050.1>.
- Kumar, A., B. Jha, Q. Zhang, and L. Bounoua, 2007: A new methodology for estimating the unpredictable component of seasonal atmospheric variability. *J. Climate*, **20**, 3888–3901, <https://doi.org/10.1175/JCLI4216.1>.
- Large, W., and S. Pond, 1981: Open ocean momentum flux measurements in moderate to strong winds. *J. Phys. Oceanogr.*, **11**, 324–336, [https://doi.org/10.1175/1520-0485\(1981\)011<0324:OOMFMI>2.0.CO;2](https://doi.org/10.1175/1520-0485(1981)011<0324:OOMFMI>2.0.CO;2).
- Larkin, N. K., and D. E. Harrison, 2002: ENSO warm (El Niño) and cold (La Niña) event life cycles: Ocean surface anomaly patterns, their symmetries, asymmetries, and implications. *J. Climate*, **15**, 1118–1140, [https://doi.org/10.1175/1520-0442\(2002\)015<1118:EWENOA>2](https://doi.org/10.1175/1520-0442(2002)015<1118:EWENOA>2).
- Lengaigne, M., E. Guilyardi, J. P. Boulanger, C. Menkes, P. Delecluse, P. Inness, J. Cole, and J. Slingo, 2004: Triggering of El Niño by westerly wind events in a coupled general circulation model. *Climate Dyn.*, **23**, 601–620, <https://doi.org/10.1007/s00382-004-0457-2>.
- Lopez, H., and B. P. Kirtman, 2014: WWBs, ENSO predictability, the spring barrier and extreme events. *J. Geophys. Res. Atmos.*, **119**, 10 114–10 138, <https://doi.org/10.1002/2014JD021908>.
- McPhaden, M. J., and Coauthors, 1998: The Tropical Ocean-Global Atmosphere (TOGA) observing system: A decade of progress. *J. Geophys. Res.*, **103**, 14 169–14 240, <https://doi.org/10.1029/97JC02906>.
- Mears, C. A., D. K. Smith, and F. Wentz, 2001: Comparison of Special Sensor Microwave Imager and buoy-measured wind speeds from 1987 to 1997. *J. Geophys. Res.*, **106**, 11 719–11 729, <https://doi.org/10.1029/1999JC000097>.
- NCEP1, 1996: NCEP/NCAR reanalysis. NOAA/Earth System Research Laboratory Physical Sciences Division, accessed 10 January 2018, <https://www.esrl.noaa.gov/psd/data/gridded/data.ncep.reanalysis.html>.
- NOAA OISST, 2002: NOAA Optimal Interpolation Sea Surface temperature version 2. NOAA/Earth System Research Laboratory Physical Sciences Division, accessed 1 February 2018, <http://www.esrl.noaa.gov/psd/data/gridded/data.noaa.oisst.v2.html>.
- Peixoto, J. P., and A. H. Oort, 1992: *Physics of Climate*. American Institute of Physics, 520 pp.
- Philander, S. G. H., and A. D. Siegel, 1985: Simulation of El Niño of 1982–83. *Coupled Ocean-Atmosphere Models*, J. Nihoul, Ed., Elsevier, 517–541.
- Reynolds, R. W., N. A. Rayner, T. M. Smith, D. C. Stokes, and W. Wang, 2002: An improved in situ and satellite SST analysis for climate. *J. Climate*, **15**, 1609–1625, [https://doi.org/10.1175/1520-0442\(2002\)015<1609:AIISAS>2.0.CO;2](https://doi.org/10.1175/1520-0442(2002)015<1609:AIISAS>2.0.CO;2).
- Ricciardulli, L., and F. J. Wentz, 2015: A scatterometer geophysical model function for climate-quality winds: QuikSCAT Ku-2011. *J. Atmos. Oceanic Technol.*, **32**, 1829–1846, <https://doi.org/10.1175/JTECH-D-15-0008.1>.
- , and —, 2016: Remote Sensing Systems ASCAT C-2015 daily ocean vector winds on 0.25 deg grid, version 02.1, period 2009–2017. Remote Sensing Systems, accessed 10 January 2018, www.remss.com/missions/ascat.
- Saha, S., and Coauthors, 2010: The NCEP Climate Forecast System Reanalysis. *Bull. Amer. Meteor. Soc.*, **91**, 1015–1058, <https://doi.org/10.1175/2010BAMS3001.1>.
- Sarachik, E. S., and M. A. Cane, 2010: *The El Niño-Southern Oscillation Phenomenon*. Cambridge University Press, 384 pp., <https://doi.org/10.1017/CBO9780511817496>.
- Schubert, S. D., M. J. Suarez, P. J. Pegion, R. D. Koster, and J. T. Bacmeister, 2004: Causes of long-term drought in the U.S. Great Plains. *J. Climate*, **17**, 485–503, [https://doi.org/10.1175/1520-0442\(2004\)017<0485:COLDIT>2.0.CO;2](https://doi.org/10.1175/1520-0442(2004)017<0485:COLDIT>2.0.CO;2).
- Seager, R., N. Harnik, W. A. Robinson, Y. Kushnir, M. Ting, H. Huang, and J. Velez, 2005: Mechanisms of ENSO-forcing of hemispherically symmetric precipitation variability. *Quart. J. Roy. Meteor. Soc.*, **131**, 1501–1527, <https://doi.org/10.1256/qj.04.96>.
- TAO/TRITON, 2000: Tropical Atmosphere Ocean/Triangle Trans-Ocean Buoy Network. NOAA/Pacific Marine Environmental Laboratory TAO project office, accessed 3 January 2018, <https://www.pmel.noaa.gov/tao/drupal//disdel/>.
- Trenberth, K. E., G. W. Branstator, D. Karoly, A. Kumar, N.-C. Lau, and C. Ropelewski, 1998: Progress during TOGA in understanding and modeling global teleconnections associated with tropical surface temperatures. *J. Geophys. Res.*, **103**, 14 291–14 324, <https://doi.org/10.1029/97JC01444>.
- Vecchi, G. A., and D. E. Harrison, 2000: Tropical Pacific sea surface temperature anomalies, El Niño, and equatorial westerly wind events. *J. Climate*, **13**, 1814–1830, [https://doi.org/10.1175/1520-0442\(2000\)013<1814:TPSSTA>2.0.CO;2](https://doi.org/10.1175/1520-0442(2000)013<1814:TPSSTA>2.0.CO;2).
- Wolter, K., R. M. Dole, and C. A. Smith, 1999: Short-term climate extremes over the continental United States and ENSO. Part I: Seasonal temperatures. *J. Climate*, **12**, 3255–3272, [https://doi.org/10.1175/1520-0442\(1999\)012<3255:STCEOT>2.0.CO;2](https://doi.org/10.1175/1520-0442(1999)012<3255:STCEOT>2.0.CO;2).
- Xue, Y., M. Chen, A. Kumar, Z.-Z. Hu, and W. Wang, 2013: Prediction skill and bias of tropical Pacific sea surface temperatures in the NCEP Climate Forecast System version 2. *J. Climate*, **26**, 5358–5378, <https://doi.org/10.1175/JCLI-D-12-00600.1>.
- , and Coauthors, 2017: A real-time ocean reanalyses intercomparison project in the context of tropical Pacific observing system and ENSO monitoring. *Climate Dyn.*, **49**, 3647–3672, <https://doi.org/10.1007/s00382-017-3535-y>.